POLITECNICO DI TORINO
Repository ISTITUZIONALE

Pore-scale modeling of fluid flow through gas diffusion and catalyst layers for high temperature proton exchange membrane (HT-PEM) fuel cells

(Article begins on next page)

Pore-scale modeling of fluid flow through gas diffusion and catalyst layers for high temperature proton exchange membrane (HT-PEM) fuel cells

Uktam R. Salomov[1], Eliodoro Chiavazzo[1], Pietro Asinari[1,*]

Multi-Scale Modeling Laboratory (SMaLL), Dipartimento Energia, Politecnico di Torino, Corso Duca degli Abruzzi 24, Zip code 10129, Torino, ITALY

Abstract

This work represents a step towards reliable algorithms for reconstructing micro-morphology of electrode materials of high-temperature proton-exchange membrane fuel cells and for performing pore-scale simulations of fluid flow (including rarefaction effects). In particular, we developed a deterministic model for a woven gas diffusion layer (GDL) and a stochastic model for the catalyst layer (CL) based on clusterization of carbon particles. We verified that both developed models accurately recover the experimental values of permeability, without any special *ad-hoc* tuning. Moreover, we investigated the effect of catalyst particle distributions inside the CL on the degree of clusterization and on the microscopic fluid flow, which is relevant for degradation modelling (e.g. loss of phosphoric acid). The three-dimensional pore-scale simulations of fluid flow for the direct numerical calculation of

---

*Corresponding author

Email addresses: `uktam.salomov@polito.it` (Uktam R. Salomov), `eliodoro.chiavazzo@polito.it` (Eliodoro Chiavazzo), `pietro.asinari@polito.it` (Pietro Asinari)

URL: `http://staff.polito.it/pietro.asinari/` (Pietro Asinari), `http://www.polito.it/small` (Pietro Asinari)

permeability were performed by the Lattice Boltzmann Method (LBM).

Keywords: High temperature PEM fuel cells, Micro-morphology of electrodes, Pore-scale modeling, Rarefied fluid flow, Kinetic theory

---

Contents

1. Introduction

Fuel cells based on proton-exchange membranes (PEM) and fueled by hydrogen and air have many attractive features, including high power den-

sity, rapid start-up and high efficiency [1]. In particular, there are several compelling reasons for operating at a temperature higher than 100 °C (HT-PEM), such as enhanced electrochemical kinetics, simplified water management and cooling and enhanced carbon monoxide tolerance [1]. On the other hand, among the major technology issues that must be addressed for their commercialization and widespread use, the degradation phenomena of the membrane electrode assembly (MEA) plays a key role [2].

Unfortunately, the failure mechanism of membranes in the PEM fuel cell is not well understood [1]. First of all, at higher operating temperature, membrane dehydration and the subsequent decrease in proton conductivity is a significant issue. Membrane dehydration results in shrinking, cracking [3] and finally in a loss of mechanical stability with increasing temperature. Moreover, an extensive morphological relaxation occurs above the glass transition temperature of a polymer (130-160 °C for a dry membrane and 80-100 °C for a hydrated membrane), which may have an adverse effect on the properties of membranes [4]. Finally, during fuel cell operation, hydroxyl radicals are responsible for chemical attack of the membrane, which initiates the degradation process [5, 6]. In the degradation of the electrodes, the issue of chemical and morphological instabilities of the catalyst layer is of greater concern at high temperatures [1]. Firstly, corrosion of the carbon support in the cathode may occur if the cathode is held at relatively high oxidation potentials because of the generation of oxygen atoms at the catalyst [7]. Secondly, the morphology of the catalyst may be affected by the agglomeration of the platinum and the increase in particle size during operation [8, 9]. The optimum particle size for oxygen reduction reaction activity is 3-5 nm [9].

Due to the increase of platinum particle size over time, the reaction rate of oxygen reduction gradually decreases, and platinum utilization is reduced. Platinum is also observed to dissolve and re-deposit during long-term operation [10]. Two mechanisms have been proposed for platinum dissolution [10], but it is not clear yet which one is more effective and how they interact during the operation.

Clearly the previous analysis points out that there is a lack of fundamental understanding of the degradation phenomena of both electrolyte membrane and electrodes for high temperature PEM fuel cells. Numerical modeling may be helpful in comparing different degradation phenomena and in quantifying the effects in terms of global device performance. One feature which is common to most of the degradation phenomena (in particular, corrosion of carbon support and catalyst agglomeration) is the change in the local morphology of the material, driven by chemical reactions and/or mechanical stresses. Modifications in the micro-morphology produce (a) *direct effects* on mass transport by changing the local porosity and permeability and (b) *indirect effects* by changing the distribution/effectiveness of reaction catalytic sites. The first step for understanding degradation consists in setting up a morphological model of the virgin micro-structure before operation, as a reference condition to compare any degradation with.

Tremendous work has been done over the past few years to visualize GDL and CL using tomography and a number of papers have been published in this area [11, 12, 13]. However, collecting a specific three dimensional morphology is different from developing a general morphological model. A specific three dimensional morphology by tomography allows one to compute precise

fluid flow through it and to find macroscopic transport coefficients. However, it does allow one to extrapolate the specific results towards different materials. On the other hand, a morphological model correlates the transport coefficients with the global microscopic structure, but it also (a) explains how different features of the microscopic structure (characteristic lengths, distributions, shapes, orientations, clustering, etc.) determine independently the transport coefficients and (b) suggests design strategies to improve transport coefficients. Hence a morphological model allows one to generate many virtual structures (all compatible with experimental data with regards to some features) in order to find out a design strategy beyond experimental measurements. For example, some PEM electrodes (and in particular the gas diffusion layers) consist of fibers which have been coated with a conductive carbon fill, leading to a highly anisotropic material without any regular micro-structure [14]. On the other hand, in the present paper, we consider gas diffusion layers for high temperature PEM fuel cells which are characterized by some degrees of regularity in the micro-structure and in the orientation of fibers. Regular materials offer better options for optimization but they are also more sensible to degradation phenomena. Hence, before developing any degradation model, the sensitivity of the macroscopic transport coefficients on the assumed micro-structure must be clarified. Moreover, concerning the catalyst layer, we used the morphological model to investigate different distributions of platinum and the consequent mass flow rate, which may affect degradation by phosphoric acid loss.

Few commercial packages are already available to generate both woven and carbon-paper GDLs. One remarkable example is given by GeoDict soft-

ware [15], initially developed by Fraunhofer ITMW. Besides the woven and non-woven fiber-based structures, GeoDict can generate a wide range of different morphologies including regular-grid, sphere packing, open- and closed-cell foams, sintered ceramic materials and their possible combinations. The results of reconstruction using both the approach proposed in this paper (see next Figure 4 (a)) and GeoDict (see Figure 2 (a) in Ref. [16]) are in good qualitative agreement. However, even though some basic ideas of GeoDict reconstruction are reported in literature [17], it is not always possible to collect enough details in order to perform a complete comparison with other methods. Moreover, as far as the authors know, there is no GeoDict specific module for reconstruction of the catalyst layer, which is our main focus here. In particular, an open and a flexible algorithm for CL reconstruction, as the one we propose in this paper, can be easily extended by considering also catalyst particles and their optimized distribution. The latter issue is essential for mitigating specific degradation mechanisms and improving cell performances (some first attempts along this direction are presented in Subsection 4.4).

Pore-scale modeling of fluid flow through electrodes has received intensive research over the past few years [18]. In particular, pseudo-kinetic (also called mesoscopic) approaches are considered efficient computational alternatives to other numerical methods. Pseudo-kinetic approaches based on the Lattice Boltzmann Method (LBM) have became very popular for simulating fluid flows [19, 20, 21, 22, 24, 23] in a variety of applications such as laminar, turbulent, thermal and multiphase flows, and even beyond hydrodynamics, according to some authors [25]. Reasons for this success are

6

attractive implementation, promising handling of complex geometries and suitability for parallel realization. Owing to its excellent numerical stability and constitutive versatility, LBM can play an essential role as a simulation tool for understanding advanced materials and processes [26]. Unlike conventional Navier-Stokes solvers, lattice Boltzmann methods consider flows as to be composed by a collection of pseudo-particles that are represented by a velocity distribution function [23]. These fluid particles reside and interact on the grid nodes. System dynamics and complexity emerge by the repeated application of local rules for the motion, collision and redistribution of these coarse-grained pseudo-particles. LBM is capable to tackle particularly those problems which are ubiquitous characteristics of flows in the world of materials science and engineering [26], including porous media with changing morphology. The lattice Boltzmann method has already proved to be an effective tool in analyzing the porous materials of fuel cells, in particular with regards to the effective permeability. This approach has been already applied to analyze the electrodes of PEM fuel cells [14, 27] and high temperature solid oxide fuel cells (SOFC) [28]. Moreover, pseudo-particles moving on regular grids can easily deal with changing morphology. To this end, it is sufficient to enable the access of pseudo-particles to new portions of the computational domain or, vice-versa, prohibit their entrance into some other computational regions (e.g. those occupied by obstacles). A recent review over the applications of LBM and other pore-scale models in fuel cells was given in Mukherjee et al. [29], which emphasizes the capability of these pore-scale models toward gaining insight into underlying two-phase dynamics and intricate structure-transport-performance interplay in the PEM fuel cell CL

and GDL.

In this paper, we focus on direct numerical simulation of the fluid flow through two fundamental regions of HT-PEM electrodes, namely a woven gas diffusion layer (GDL) and a catalyst layer (CL). We believe that focusing on fundamental modeling of materials for HT-PEM fuel cells may promote the development of this technology, as already happened for other types (e.g. solid oxide fuel cells). Moreover, HT-PEM fuel cells usually involve materials with regular micro-structure, where morphological models can be tuned in order to recover the macroscopic transport properties. These validated morphological models can be used in order to feed macroscopic models by material-depending parameters [30], to guide the material production process and to understand degradation phenomena.

The paper is organized as follows. In Section 2, a brief description of the adopted methodology (including boundary conditions) is presented a simple validation is reported in Appendix A). In Section 3, we report the reconstruction of two regions (GDL and CL) of the HT-PEM electrodes by analyzing realistic micro-morphologic images. In Section 4, the results of pore-scale flow simulations through these porous media using the previous methodology and the effective permeability, calculated by the Darcy's law and taking into account also rarefaction effects are presented. Moreover, the influence of catalyst distribution on mass transport properties is considered in this section. Some conclusions and outlines are reported in the final section.

8

2. Lattice Boltzmann Method

The Lattice Boltzmann Method (LBM) was derived historically as an improvement of the Lattice Gas Automata (LGA) [23] and it can be derived from kinetic theory of gases, under some proper simplifying assumptions [24]. It should be emphasized that, in spite of these origins, as far as the present work is concerned, we will use this method as a computational solver of the continuum-based equations for solving the pore-scale fluid flow through porous media. Rarefaction effects will be taken into account by properly post-processing the previous numerical results (see Subsection 4.3).

In this paper, LBM is preferred to other computational fluid dynamics (CFD) solvers, because of two advantages which are relevant to the present application. The first one is a reasonable handling of complex geometry of porous media, which is consistent with the main objectives of this work, where we need to consider the detailed structure of two layers of high temperature PEM (HT-PEM), namely gas diffusion layer (GDL) and carbon supported catalyst layer (CL). The second advantage is a good parallelization potential, owning to an explicit formulation of the evolution operator $\mathcal{E}$ in terms of the discrete distribution function $f(\mathbf{x}, t)$, which can be interpreted in terms of Strang splitting [31]:

$$f(\mathbf{x} + \xi, t + 1) = \mathcal{E}f(\mathbf{x}, t) = \mathcal{S}\mathcal{C}f(\mathbf{x}, t), \tag{1}$$

consisting of a fully local collision operation $\mathcal{C}$ and a streaming operator $\mathcal{S}$, involving only the neighbouring nodes.

The simplest choice for the collisional operator $\mathcal{C}$ corresponds to the popular Bhatnagar-Gross-Krook (BGK), developed in kinetic theory [32], and

9

successfully applied in the LBM context as well [22]. The BGK model can be further simplified by considering isothermal conditions, constant relaxation time and formulating it only for the lattice velocities, namely

$$f_i(\mathbf{x} + \xi_i, t + 1) = f_i(\mathbf{x}, t) + \frac{1}{\tau} \left(f_i^{eq}(\mathbf{x}, t) - f_i(\mathbf{x}, t) \right), \tag{2}$$

where ξ_i denotes the i-th discrete velocity, τ is the relaxation time, while f_i^{eq} is the equilibrium population function, which can be obtained from the local Maxwell-Boltzmann distribution function (see for example [24]) by Taylor expansion. Equilibrium discrete distribution functions, i.e. equilibria, for the $D3Q19$ model read as follows:

$$f_i^{eq} = W_i \rho \left(1 + \frac{1}{c_s^2} (\xi_i \cdot \mathbf{u}) + \frac{1}{2c_s^4} (\xi_i \cdot \mathbf{u})^2 - \frac{1}{2c_s^2} (u^2) \right), \tag{3}$$

where W_i and ξ_i are the weight factors and particle velocities, respectively, with $c_s = 1/\sqrt{3}$ being the speed of sound. It can be shown that the lattice Boltzmann equations (2) recover Navier-Stokes equations in the asymptotic limit. This derivation can be done using the Chapman-Enskog expansion [33] or the Hilbert expansion, also called asymptotic analysis, which has the merit to make particularly evident the effects due to different scaling assumptions, i.e. how lattice velocity is set according to the grid spacing on different grids [34].

Probably one of the most appealing features of LBM consists in the possibility to use the bounce-back rule as no-slip boundary condition (BC), which allows one to consider obstacles with complex shape into the fluid domain in a simple manner [23]. For any boundary node $\mathbf{x}_w$ and direction i such that the node $\mathbf{x}_w + \xi_i$ does not exist because it is outside the computational

10

domain, the bounce-back rule is the following:

$$f_{BB(i)}(\mathbf{x}_w, t+1) = f_i^*(\mathbf{x}_w, t), \tag{4}$$

where $BB(i)$ is the lattice index identifying the lattice velocity $\xi_{BB(i)}$ which is opposite to ξ_i, namely $\xi_{BB(i)} = -\xi_i$, and f_i^* is the post-collision discrete distribution function, namely $f_i^* = f_i + (f_i^{eq} - f_i)/\tau$. Standard bounce-back BC reproduce macroscopic no-slip wall boundary condition with first-order accuracy in time and space [35]. Higher accuracy has been achieved considering the wall-fluid interface to be located half-way between the wall and the fluid lattice nodes [36]. Further improvement is given by generalizing the previous expression such that the wall location can be freely tuned [37].

3. Micro-morphology reconstruction

3.1. Preparation of the Membrane-Electrode-Assemblies

In this work, we considered a high temperature polymeric electrolyte membrane (HT-PEM) fuel cell $Celtec - P1000$ manufactured by BASF$^{©}$. A membrane electrode assembly (MEA) is made as follows (according to Ref. [38]): On top of a woven (carpet-like) gas diffusion layer (Toray Graphite Paper, TGPH-120, BASF Fuel Cell, Inc.), a micro-porous layer is deposited, consisting of Vulcan $XC - 72R$ Carbon Black (Cabot Corp.) and polytetrafluoroethylene (Teflon$^{®}$ Emulsion Solution, Electrochem Inc.). Moreover, a catalytic layer is also deposited, composed of Platinum (Pt) catalyst on carbon (C) support (Pt on Vulcan XC-72R Carbon Black, ETEK-Inc.). A typical schematic diagram of a polymer electrolyte membrane fuel cell MEA together with two main electrochemical reactions during fuel cell operation,

hydrogen oxydation (HOR) in anod catalyst layer and oxygen reduction (ORR) in cathode catalyst layer, are illustrated in Fig. 2.

Our modeling activity starts from Scanning Electron Microscope (SEM) micro-morphology images of the above HT-PEM fuel cell reported in Fig. 1, which are original and purposely obtained for this goal. The considered system consists of an impermeable (for the gases) electrolyte at the center (Fig. 1 (a) and (c)), with two very thin regions at the upper and bottom sides of the electrolyte, sandwiched between the electrolyte and the electrodes. These regions are the carbon supported Pt catalyst layers (Fig. 1 (d)), which hold together the membrane and two (anode and cathode) woven gas diffusion layers (Fig. 1 (a) and (b)). The most significant geometrical parameters of the system are given in Table 1.

Two options are typically possible when dealing with modeling of complex media. One option is to obtain directly 3D information. The advent of dual-beam focused ion beam scanning electron microscopy (FIB-SEM) has greatly facilitated this process by providing high-quality volumetric data [42]. However, image analysis techniques remain nowadays the most popular because of the low cost of equipments and instrumentations, which have already large-diffusion [43]. In this paper, we will focus on the latter approach, which is based on post-processing 2D SEM images in order to get the most meaningful topological information. The considered materials are characterized by a regular micro-structure (in particular GDL), which makes the development of morphological models (depending on few parameters) possible.

We have performed pore-scale reconstructions of the microscopic topology of the system using information given in Table 1 and micro-morphology

images (Fig. 1). This has been done in order to define realistic paths for the pore-scale fluid flow. To this purpose, a digital map of the whole geometry is collected in a one dimensional array, whose elements correspond to the mesh nodes. Three possible values are assigned to the array elements, 0 for fluid, 2 for solid and 1 for boundaries between solid and fluid. Tracing the interface between solid and fluid nodes is useful for applying boundary conditions (e.g. the bounce-back rule discussed in the previous Section 2). The one dimensional array can be reported mathematically by the following definition

$$\mathcal{M}_{i_x,i_y,i_z} = \begin{cases} 0 & (i_x, i_y, i_z) \in fluid \\ 1 & (i_x, i_y, i_z) \in fluid \bigcap solid \\ 2 & (i_x, i_y, i_z) \in solid \end{cases} \tag{5}$$

In the following two subsections, the details on how to generate the arrays $\mathcal{M}_{GDL}$ and $\mathcal{M}_{CL}$ for GDL and CL respectively, which represent the geometries of reconstructed porous media, are reported. It should be noted that topology reconstruction of the different layers (GDL and CL) has to be considered separately, due to the considerable disparity in reconstruction algorithms and characteristic scales of their geometry.

3.2. Reconstruction of a woven GDL

Let us start with reconstruction of a woven gas diffusion layer, similar to the one depicted in Fig. 1, whose characteristic cell consists of four orthogonal bundles of fibers. For simplicity, we have considered the $x-$direction as the main flow direction, consequently $yz-$plan is a woven plane (see Fig. 3 for details). The following assumptions are considered in the main reconstruction algorithm:

13

(i) Fibers of the GDL are grouped into two pairs of mutually orthogonal bundles;

(ii) A cross-section of a bundle is an ellipse with L_A and L_B, being semi-major and minor axes, respectively;

(iii) Fibers are homogeneously distributed in a bundle;

(iv) A fiber is modeled as a cylinder with sinusoidal directrix.

The suggested reconstruction procedure starts with the estimate of the average distance d between two nearest neighbor fibers within a bundle and the radius of fibers r. These parameters can be obtained by analyzing the images in Fig. 1 and using simple geometric relations, namely

$$d = \frac{1}{2}\left(\frac{L_A}{N_A} + \frac{L_B}{N_B}\right) - 2r, \tag{6}$$

$$r = \left(\frac{(L_A N_B + L_B N_A)^2}{4\pi N_A^2 N_B^2}\frac{4(N_A - 1)(N_B - 1)}{4(N_A - 1)(N_B - 1) - N_t} \right.$$
$$\left. -\frac{L_A L_B}{4(N_A - 1)(N_B - 1) - N_t}\right)^{1/2}, \tag{7}$$

where N_A, N_B and N_t are number of fibers along semi-major axes, semi-minor axes and total number of fibers in an elliptic bundle, respectively. An example of reconstructed woven GDL is reported in Fig. 4.

For the values of $N_A = 18$, $N_B = 12$, $L_A \approx L_z/4 = 240\,\mu m$, $L_B \approx L_x/4 = l_{GDL}/4 = 100\,\mu m$ (taken by analyzing Fig. 1 (a)), we have obtained $d = 3.7\,\mu m$ and $r = 3.5\,\mu m$. Hence, for the sake of simplicity, $d \approx r$ has been assumed in the following calculations. The above few parameters are

14

enough for reconstructing 3D micro-morphology of GDL, because the latter clearly shows some degree of regularity. Due to orthogonality (see the above assumption (i)), 3D reconstruction can be easily done by generating first fibers along y-direction and consequently generating, in a similar way, the orthogonal fibers along the z-direction. Concerning the y-fibers, let us generate first (a) one 2D slice (xz planes in Fig. 3 (a)) at the generic side of the computational box, (b) one 2D slice at the middle and (c) one 2D slice at the opposite side. All remaining slides are created by changing the coordinates of the centers of fiber sections along sinusoidal directrix during the final step (d). Hence let us define the 3D reconstruction algorithm of a woven GDL porous medium according to the following steps:

- Creation of an elliptic bundle of circular fiber sections with a given radius;

- Creation of a 2D slice by merging two elliptic bundles (Fig. 3 (a));

- Creation of all 2D slices (including those depicted in Fig. 3 (b) and (c)) by shifting the centers of fiber sections along sinusoidal directrix (Fig. 3 (d)). Notice that inside each slice there are two directrixes, which are shifted by half wave length;

- Creation of the orthogonal fibers in a similar way and assembly of the reconstructed 3D micro-structure.

Finally, the resulting porosity ε of the reconstructed geometry has been compared to the reference values [39, 40]. To this end, ε can be calculated as a ratio between the volume occupied by fluid V_f and the total volume V_d of

15

the computational domain:

$$\varepsilon = \frac{V_f}{V_d} = \frac{V_d - V_e}{V_d}, \tag{8}$$

where V_e is the volume occupied by obstacles. The total volume of the computational domain is $V_d = L_x L_y L_z$, while the volume of fibers in GDL can be calculated using the following expression:

$$V_e = N_b N_t V_{se} = N_b N_t \pi r^2 \int_0^{L_x} \sqrt{1 + f'(x)^2} \, dx, \tag{9}$$

where N_b and N_t are the number of bundles in the considered woven geometry and the number of fibers in a single bundle, respectively. According to the assumption (iv), $f(x) = \sin x$. As a result, porosity of the reconstructed 3D porous medium is $\varepsilon = 0.6892$, for the following set of parameters $N_b = 4$, $N_t = 400$, $N_y = N_z = 1112$ and $N_x = 432$, which is close to the experimental value of $\varepsilon_{GDL} = 0.7$ (see Table 1).

3.3. Reconstruction of CL

The reconstruction procedure of the catalyst layer micro-morphology is different from the one of GDL due to the lack of regularity of such porous medium. In Table 1, major parameters of carbon support of catalyst can be found, such as length of the catalyst layer $l_{CL} = 30 \, \mu m$ and the average size of carbon particles around $D_{cp} = 30 - 40 \, nm$ (these data can also be estimated by analyzing Fig. 3 about Vulcan XC-72 in Ref. [44]). Here, we focus on algorithms which can accurately describe the CL morphology (see Fig. 3 in [44]) for a given porosity parameter $\varepsilon_{CL} = 0.5 - 0.6$ (as reported in the Table 1). The first straightforward approach consisted in randomly placing spheres with a fixed radius in the computational domain. To this end, the number

16

of particles N_{cp} has to be estimated as a function of porosity. In particular, percolation theory [45] predicts that:

$$\varepsilon_{CL} = e^{-nV_{cp}}, \tag{10}$$

where n is the volume concentration of carbon support particles (i.e. spheres), and V_{cp} the volume of each particle. In our simulation, the computational domain is a cube with edge $L_x = L_y = L_z = L$ and volume $V = L^3$, whereas the volume of a single carbon support particle is $V_{cp} = \frac{4}{3}\pi R_{cp}^3$ with $n = N_{cp}/V$ and

$$N_{cp} = \frac{3ln(1/\varepsilon_{CL})}{4\pi}\left(\frac{L}{R}\right)^3. \tag{11}$$

We find out that the above straightforward approach, in the subsequent direct numerical simulations (see Section 5), produces a value of permeability of $k_{single} = 1.07451 \times 10^{-16}\, m^2$, namely three orders of magnitude smaller than the real value of permeability $k_{CL} = 1 \times 10^{-13}\, m^2$ (see Table 1).

The source of a such mismatch lies in the incorrect reconstruction of the catalyst layer. This also confirms that finding a suitable model for micro-morphology is far from trivial. In fact, as it can be seen from the real micro-morphology (see Fig. 3 in Ref. [44]), the assumption of homogeneously distributed particles within the carbon supported catalyst layer is not realistic. A more accurate inspection of real micro-morphology reveals a structure where carbon particles are clustered into groups with some characteristic size $L_{cluster}^{av}$. The above mismatch induced us to re-design the algorithm of CL reconstruction, taking into account clusterization of carbon support particles, as well. To this end, CL is assumed to be formed by randomly generated 3D clusters of ellipsoidal shape, containing spherical carbon support particles.

17

For the sake of completeness, below we summarize the adopted assumptions in the modified reconstruction algorithm:

(i) A simple cluster is an ellipsoid containing spherical carbon support particles;

(ii) Irregularity of the shape of each cluster is provided by random generation of semi-axes A and B of the ellipsoid, while the third semi-axis C is calculated preserving a fixed average cluster volume;

(iii) Each cluster is filled by random deposition of spherical carbon particles inside it;

(iv) Random orientation of the ellipsoid is obtained by random rotations around the three coordinate axes.

The new algorithm for reconstructing the CL geometry, taking into account all above assumptions, is presented below:

- Random generation of ellipsoid center coordinates $(x_0^c,\ y_0^c,\ z_0^c)$;

- Random generation of N_{cp} coordinates of the centers of spherical carbon particles $(x_0^i,\ y_0^i,\ z_0^i)$ around $(x_0^c,\ y_0^c,\ z_0^c)$. The number of carbon particles within a single cluster N_{cp} can be calculated by:

$$N_{cp} \approx \frac{ABC}{R_{cp}^3},$$

where R_{cp} is an average size of carbon particles. It should be noted that, in order to fulfill assumption (i), only carbon particles whose center satisfies the following inequality are counted:

$$\frac{(x_0^i - x_0^c)^2}{A^2} + \frac{(y_0^i - y_0^c)^2}{B^2} + \frac{(z_0^i - z_0^c)^2}{C^2} \leq 1;$$

18

- Repetition of above two steps $N_{cluster}$ times, which can be found using percolation theory and assumption (iii), namely

$$N_{cluster} = \frac{3\ln(1/\varepsilon_{CL})}{4\pi} \left(\frac{L}{L_{cluster}^{av}}\right)^3.$$ (12)

The previous refinement of the morphological model of a catalyst layer, based on the degree of clustering, definitely improved the match with experimental permeability (see in details Section 4). However, it leaded to overestimation of real clusterization, which was further improved by redistributing Pt catalyst inside CL (Subsection 4.4).

4. Direct numerical simulation of permeability

For all the following fluid flow simulations, the BGK collisional operator in the LBM solver has been used. However, it should be emphasized that this approach, in spite of its simplicity, has some drawbacks, such as the dependence of permeability on relaxation frequencies [35]. In the paper by Pan et al. [35], these effects have been analyzed in detail and it was found that relaxation frequency in the BGK-LBM approach considerably affects the computed permeability. In particular, an increase of relaxation time leads to an approximately linear increase of permeability for the same geometrical configuration of porous medium, which is clearly unphysical. However, this effect almost vanishes for the value of relaxation time $\tau = 1\, l.u.$ (lattice units). This encouraged us to choose the latter value of viscosity in order to increase the accuracy of our computations, instead of considering a more complex collision model as the multiple-relaxation-time (MRT) model [14, 35, 46].

We have applied periodic boundary condition in the y- and z-direction, while, along the $x-$direction, inlet and outlet pressure difference was applied by imposing P_{inlet} and P_{outlet} respectively (see Fig. 4). Bounce-back boundary condition has been considered to model no-slip wall boundaries between fluid and solid obstacle (fibers or particles). Permeability k of porous medium has been computed according to its conventional definition imposing constant pressures at the opposite sides of porous media and using the Darcy's law, namely

$$k = \frac{\rho u \nu}{\partial P / \partial x}.$$ (13)

Recalling that the Darcy's law is valid only for laminar flows, we repeated the simulations for excluding any dependence of the computed permeability on the imposed pressure differences and consequently on the mean flow velocity. Therefore, we run each simulation several times at different pressure differences: $\Delta P = P_{inlet} - P_{outlet} \in [0.0001, 0.0005, 0.005]\, l.u..$ For all these values, we obtained the same permeability, which proves that basic assumptions underlying the Darcy's law are indeed valid.

4.1. Results of fluid simulation in GDL

Firstly we have computed the fluid flow through a gas diffusion layer of the HT-PEM, reconstructed as described in the previous Section, in order to evaluate permeability. In the direction orthogonal to the main flow, periodic boundary conditions are applied. Hence the computational domain consists of one periodic elementary cell of the woven structure. All geometrical features of the porous medium (namely radius of cross-section of electrodes r, distance between neighbor electrodes d, edges of computational domain L_x,

20

L_y, L_z, mesh spacing Δx) have been re-parametrized by a dimensionless resolution parameter n_r. In particular, we have assumed $L_y = L_z = 278\, n_r\, \Delta x$ and $L_x = 108\, n_r\, \Delta x$ and $r = d = n_r\, \Delta x$. Here, it should be noted that the condition $n_r \geq 3$ is required to have (at least) one fluid node between two neighboring fibers in a bundle. In particular, the following simulation is carried out with $n_r = 4$ and $N_t = 400$. The numerical results for pore-scale fluid flow through the reconstructed GDL are given in Table 2. The computed value of permeability, namely $k_{GDL} = 0.443638 \times 10^{-12}\, m^2$, is in good agreement with the experimental values (see Table 1). It is important to point out that no special tuning was applied in order to achieve this result.

We notice that a DELL Precision® T7500 Linux workstation was not suitable to perform simulation in this case (see Appendix about validation). In fact, in a 32 bit floating-point representation, the single computational node with a $D3Q19$ lattice requires 76 $(19 \times 32/8)$ bytes. The requirement $n_r \geq 3$ implies at least $324 \times 834 \times 834 \times 76 \approx 16\,\mathrm{GB}$ of RAM. Therefore, this simulation has been performed by a small Transtec® HPC cluster with 72 total virtual cores, 144 GB total RAM, 5.5 TB total disk capacity (3.0 TB failure free), double networking by both Infiniband and GBit. This cluster has 8 computational nodes with following properties: 2 Quad-core Intel Xeon, 2.33 GHz processors, corresponding to 8 virtual cores; 16 GB RAM, leading to 2 GB/core ratio; 250 GB SATA hard drive, 7200 rpm. The previous simulation for computing permeability with $n_r = 4$ required the full computational power of the cluster. Efficient implementation of Lattice Boltzmann schemes is discussed in Ref. [47]. Information about the specific efficiency of Palabos code for different architecture and number of cores is

4.2. Results of fluid simulation in CL

In this case, a more sophisticated reconstruction of micro-morphology has been developed. The additional computational requirement was fully compensated by relatively less demanding flow simulation. In Table 3, the sensitivity of permeability on the cluster size of carbon particles is reported. For all simulations, we used a cubic computational box made of $N \times N \times N$ nodes and porosity $\varepsilon_{CL} = 0.5$. Random deposition of carbon particles, performed using the first straightforward approach (see previous Section about reconstruction), leads to permeability, which is approximately three orders of magnitude smaller than the real value. On the other hand, following the refined approach, clusterization provides a considerable improvement in predicting the real permeability, as far as the optimal value $L^{av}_{cluster} = 1500\,nm$ is used. Notice, this value of clusterization is too high, according to very recent experimental results [13]. The reason is due to the assumption that all catalyst particles deposited on the bottom of CL, which we made for calculation of permeability using conventional approach. While in reality catalyst particles are widespread in CL and the distribution of them considerably affects to mass flow rate (see Subsection 4.4).

In Fig. 5, the reconstructed geometry and the flow streamlines through the CL porous medium are reported, using both straightforward approach (results (a) and (b)) and refined approach taking into account clusterization (results (c) and (d)). A magnification of fluid flow simulation based on the first approach (see Fig. 5 (b)) is intended to make more visible the fluid paths: fluid flow is dispersed in the porous medium and hence it is highly reduced

because of drag resistance. On the other hand, in the refined approach (see Fig. 5 (d)), because carbon clusters are impermeable for fluid, the fluid flow can take advantage of the interstices among clusters.

4.3. Rarefaction effect

In the previous subsections, the continuum-based equations, i.e. incompressible Navier-Stokes equations, were used for solving the pore-scale fluid flow through porous media. However some of the pores have a characteristic size which is comparable with the mean free path of the gas λ, i.e. the average distance traveled by a gas particle between two subsequent collisions. Fluid flow with length scales of the order of the mean free path of fluid particles is characterized by rarefaction effects which are not properly described by standard hydrodynamics based on continuum equations [49]. Hence, in this subsection, we investigate on possible rarefaction effects, in order to find out if they may eventually modify in a substantial way the previous permeability estimates and consequently the reliability of reconstructed morphological models.

The fundamental dimensionless number for describing the rarefaction effects is the Knudsen number Kn [49, 50], defined as the ratio between the mean free path of the gas λ and a macroscopic length L_{char} describing the flow, e.g. a channel width or the diameter of an object exposed to the flow, namely

$$Kn = \frac{\lambda}{L_{char}}. \tag{14}$$

The Navier-Stokes equations are applicable only for flows at sufficiently small Knudsen numbers and fail in the description to flows at Knudsen numbers

$Kn > 0.01$ [49, 51, 52]. In particular, depending on the Knudsen number, there are many flow regimes: Continuum flow ($Kn < 0.01$); Slip-flow ($0.01 < Kn < 0.1$); Transient flow ($0.1 < Kn < 3$); Free molecular flow ($Kn > 3$).

In order to estimate the Knudsen number in our simulations, we have to calculate both the mean free paths for the gases involved in electrochemical reactions of the HT-PEM and the characteristic lengths of the considered porous media, i.e. GDL and CL. For the sake of simplicity, let us consider separately the mean free paths of the single components of the reactive mixture in the ideal case, namely hydrogen, oxygen and water vapor. This simplifying assumption will be enough for finding out the relevant order of magnitude. According to the standard theory of ideal gases [53], the mean free path can be computed as

$$\lambda = \frac{1}{\sqrt{2}\pi\,d^2\,n},$$
(15)

where n is the number of molecules per unit volume and d is the molecular diameter. Moreover, the kinematic viscosity ν can be computed by the Maxwell's formula [53], namely

$$\nu = \frac{2}{3\pi\,d^2\,n}\sqrt{\frac{k\,T}{\pi\,m}},$$
(16)

where $k = 1.3087 \times 10^{-23}\ J/K$ is the Boltzmann constant, T is the operating temperature and m is the mass of the molecule. Combining the previous formulas yields

$$\lambda = \nu\,\frac{3}{2\sqrt{2}}\sqrt{\frac{\pi\,m}{k\,T}}.$$
(17)

Taking data about transport coefficients from NIST database [54] and using the previous formula given by Eq. (17), it is possible to estimate the mean

free paths for the gases involved in electrochemical reactions of the HT-PEM, as reported in Table 4. The mean free paths under operating conditions of temperature $T = 423\,K$ and pressure $P = 101325\,Pa$ are $159\,nm$, $270\,nm$ and $113\,nm$ for oxygen, hydrogen and water (vapor), respectively. In the following calculations, the mean free path of hydrogen will be used in order to check the sensitivity of the computed permeabilities with regards to the highest Knudsen number.

Concerning the characteristic lengths of the considered porous media, we propose the following simplified procedure. The pressure gradient through a straight capillary is given by the standard Hagen-Poiseuille equation [55], namely

$$\frac{\partial P}{\partial x}\bigg|_{HP} = -\frac{32\mu u}{L_{char}^2}, \tag{18}$$

where, in this case, L_{char} is the capillary diameter. The previous formula can be generalized in case of porous media [56] in the following way

$$\frac{\partial P}{\partial x} = \frac{\partial P}{\partial x}\bigg|_{HP} \frac{h'/h}{\varepsilon} = -\frac{32\mu u}{L_{char}^2} \frac{h'/h}{\varepsilon}, \tag{19}$$

where h is the straight path (minimum length) through the porous medium and h' the actual path. Sometimes the ratio h'/h is called tortuosity in the literature on porous media [56]. A typical value of $h'/h = 5/2$ is often encountered dealing with fuel cells and this is in good agreement with direct numerical simulations of fluid flow in fuel cell electrodes [28]. Assuming $h'/h = 5/2$ and combining the previous equation with the Darcy's law given by Eq. (A.1) yields

$$L_{char} = \sqrt{\frac{80\,k}{\varepsilon}}, \tag{20}$$

where k is the permeability of the porous medium computed with no-slip boundary conditions, i.e. without rarefaction effects.

In order to calculate how rarefaction affects the permeability, we use the results of a previous study about pressure-driven flow through a microchannel [57]. In Ref. [57], the two-dimensional isothermal flow in case of low Mach number $Ma \ll 1$ and moderate Knudsen number $Kn \leq 0.15$ is analyzed by using the Navier-Stokes equations with a first-order slip-velocity boundary condition. In particular, by means of a perturbation expansion in the height-to-length ratio of the channel and using the ideal gas equation of state, the zeroth-order analytic solution for the stream-wise mass flow rate is derived. In the original Ref. [57], the stream-wise mass flow rate is expressed in terms of the two-dimensional Knudsen number $Kn_H = \lambda/H$ where H is the channel height. The channel height H is actually half of the hydraulic diameter, which is the proper characteristic quantity for describing both two- and three-dimensional flows, i.e. $H = L_{char}/2$. Consequently $Kn_H = 2\,Kn$ where $Kn = \lambda/L_{char}$ as usual in the present paper. Taking into account this generalization for three-dimensional flows and recalling Eq. (A.1), the original formula for the stream-wise mass flow rate can be used for deriving an expression of permeability correction as a function of Kn, namely

$$\frac{k_{slip}}{k_{no-slip}} = 1 + \frac{24\,\sigma\,Kn}{1 + \mathcal{P}},\tag{21}$$

where k_{slip} is the permeability taking into account the rarefaction effects, $k_{no-slip}$ is the permeability computed as in the previous subsections, σ is the momentum accommodation coefficient, which depends on the properties of porous medium (for engineering calculation usually $\sigma = 1$) and $\mathcal{P}$ is the ratio between inlet and outlet pressure, i.e. $P_{inlet}/P_{outlet} \geq 1$. In deriving both

26

numerical results for GDL, reported in Table 2, and those for CL, reported in Table 3, a pressure ratio equal to $\mathcal{P} = 1.0005$ was used.

The previous expression represents the last ingredient for taking into account the rarefaction effects. The proposed simplified procedure is the following: By Eq. (20), the characteristic length L_{char} is derived for a given porous medium with an already computed no-slip permeability; Consequently the Knudsen number $Kn = \lambda/L_{char}$ is computed; Finally, by Eq. (21), the permeability correction, i.e. $k_{slip}/k_{no-slip}$, is computed and allows one to derive the refined estimate of permeability, accounting for rarefaction effects. In Table 5 an estimate of the rarefaction effects on the calculation of permeability for both GDL and CL is presented for hydrogen (having the highest Knudsen number, as reported in Table 4). Clearly, according to these precautionary estimates, the rarefaction effects are not negligible in general for the present porous media. These estimates are the highest expected deviations from the results reported in the previous subsections. However it is worth the effort to point out that, even in the worst case, i.e. a permeability increase of a factor of two for CL, the latter is still quite smaller than the dependency of predicted permeability on the underlaying morphological model. In fact, in Table 3, changing the average size of cluster from $400\,nm$ to $1500\,nm$ leads to an increase of the permeability of one order of magnitude (five times the previous maximum rarefaction effect). Moreover, taking $k_{no-slip} = 0.420467 \times 10^{-13}\,m^2$ from the last row of Table 3 and multiplying it by $k_{slip}/k_{no-slip} = 2.249$ leads to an effective permeability of $k_{slip} = 0.945567 \times 10^{-13}\,m^2$, which is pretty close to $1 \times 10^{-13}\,m^2$ reported in Table 1. Hence the developed morphological models can be considered robust against rarefaction effects.

4.4. Effects of platinum particle distribution in CL

In this section, we explore some catalyst layer configurations by tuning the distribution of the catalyst Pt particles. The goal is twofold. First of all, the assumption of placing all catalyst Pt particles at the interface between CL and membrane is not realistic (even though imposing constant pressures at the opposite sides of porous media is the standard way to compute permeability according to its conventional definition). The reason is that conventional definition of permeability (see Eq. (13)) does not rigorously apply to CL, where electrochemical reactions happen inside the layer itself. The conventional definition may lead to an underestimation of the effective pressure gradient and consequently an overestimation of the particle clustering, in order to recover the same experimental permeability (as we did in Subsection 4.2). This is why, in our calculations, we found a particle clustering higher than what it should be, according to some very recent tomography data [13]. More specifically, it should be noted that Darcy's law for permeability calculation assumes that all sink nodes (Pt particles) are deposited at the domain bottom side. However, in real systems, catalyst particles are spread homogeneously inside catalyst layer, where the electrochemical reactions take place. Hence the real partial pressure gradient due to electrochemical reactions is actually smaller than the simulated one. In this section, we explore the sensitivity of numerical results on this assumption.

Secondly, the catalyst particle distribution should be optimized in order to improve the performance of the PEMFCs and also to mitigate degradation mechanisms (e.g. loss of phosphoric acid). Optimal functionalization of catalyst layer can be achieved by proper tuning mass transport properties of

28

CL microstructure with regards to transport of reactant (hydrogen, oxygen) and product gases (water vapour). In this stage, the role of the proposed morphological model is essential. From the morphological point of view, it is important to have small platinum particles with large surface area, finely dispersed on the catalyst support surface (typically carbon powders). Large amount of work has been done during last years to decrease the platinum loading on the catalyst layer, using advanced catalyst deposition techniques or promoting platinum alloys with other metals, e.g. Pt-Ru, Pt-Sn, Pt-Cr. However mainly the fraction of Pt particles on the carbon support of PBI-based high temperature PEMFC has been considered so far. Thus, electrodes with different platinum percentages on the carbon support, but with the same PBI content normalized with respect to the C/PBI weight ratio (C/PBI = 20), have been treated and optimal weight ratio has been found [38].

In the present work we investigated an influence of Pt deposition on the mass flow rate through the same porous medium. We slightly extended our previous model for reconstruction of CL microstructure by introducing a new discrete value in Eq. 5 for one dimensional array describing the geometry. For example, let us assume $\mathcal{M} = 3$ for Pt catalyst particles in catalyst layer, namely

$$
\mathcal{M}_{i_x, i_y, i_z} = \begin{cases} 0 & (i_x, i_y, i_z) \in fluid \\ 1 & (i_x, i_y, i_z) \in fluid \bigcap solid \\ 2 & (i_x, i_y, i_z) \in solid \\ 3 & (i_x, i_y, i_z) \in catalyst\ particles \end{cases} \tag{22}
$$

For comparison, we considered two simulation setups illustrated in Fig.6 (a) and (b), where the same amount of catalyst particles is used, but by different

distributions reported in 6 (c) and (d). In particular, the former distribution is the conventional one used to compute permeability by Darcy's law, while the latter has been obtained by redistributing platinum particles inside the catalyst layer.

Pore-scale simulations using BGK lattice Boltzmann method were performed for catalyst layers with clusterization equal to $L_{av} = 1500nm$ and with the previous Pt deposition distributions. It should be noted, for the all simulation imposed pressure difference was taken $\Delta P = 0.00001$ in order to be sure that flow is indeed laminar. In Table 6, the parameters of porous medium, computational domain, lattice Boltzmann method and the mass flow rate at the inlet are reported. As it can be seen from the table, we have approximately an order of magnitude increase in flow rate by redistributing Pt particles. Mean velocity and flow rate change (see Fig.7 (c-d)), but also fluid flow streamlines change (see Fig.7 (a-b)). This means that there are quantitative changes (scale factor), but also qualitative changes in the flow field. Thus, redistribution of catalyst particles inside the microstructure leads to considerable increase of mass flow rate and it provides an additional tunable parameter of the morphological model.

The morphological model proposed in this paper allows one to explain how macroscopic transport coefficients are sensitive to different features of microstructure, like carbon support clustering and catalyst distribution. The latter point is very relevant also for analyzing three dimensional morphology by tomography. In fact, computing permeability of tomography microstructure by assuming catalyst on the bottom side would lead to inaccurate results, in spite of the accuracy on the geometry. This proves that any input

30

data about morphology must be interpreted by a morphological model. The morphological model presented here may be useful for designing strategies in order to increase PEMFC performance and to mitigate degradation phenomena by improving mass transport processes.

The main idea behind the mitigation strategy is to manipulate flow field through catalyst layer by realizing different setups of morphological parameters, like distribution of catalyst particles, clusterization and so on. As a concluding remark, let us consider a simple example. It is reasonable to assume that the loss of phosphoric acid at the interface between catalyst layer and the membrane is also driven by the normal pulling stress. The latter is proportional to the normal velocity gradient. Hence the pulling stress could be reduced by properly placing the catalyst particles, e.g. by an exponential decay distribution with flatter profile at the above mentioned interface. The systematic and comprehensive results about the application of the developed morphological model to mitigate specific degradation mechanism, i.e. phosphoric acid loss from membrane and catalyst layer (without significant changes in current density), will be presented elsewhere.

5. Conclusions

Operating PEM fuel cells at high temperature is definitively a promising technology, because of enhanced electrochemical kinetics, a simplified water management and cooling and the enhanced carbon monoxide tolerance. However the degradation phenomena of the membrane electrode assembly (MEA) represents one of the major issues that must be addressed for their commercialization and widespread use. Understanding detailed degradation

phenomena will require a huge community effort. However we think that pore-scale modeling, simulation and morphological models can be definitively powerful tools towards this goal. The present paper represents a preliminary step towards reliable algorithms for reconstructing micro-morphology of HT-PEM electrodes. Pore-scale modeling has already boosted the technological development of other types of fuel cells, e.g. solid oxide fuel cells, where many contributions have been observed in recent years. Moreover, this kind of modeling techniques can take strong advantage by recent progresses in dual-beam focused ion beam scanning electron microscopy (FIB-SEM). However, it must be pointed out that developing reliable morphological models is essential for interpreting the morphological data by FIB-SEM.

In this paper, we focus on direct numerical simulation of the fluid flow through two fundamental regions of HT-PEM electrodes, namely a woven gas diffusion layer (GDL) and a catalyst layer (CL). The considered woven GDL is characterized by a regular micro-structure, where morphological models depend on few parameters that can be set by inspection of images obtained by scanning electron microscopy. On the other hand, permeability through CL is highly sensible to clusterization of carbon particles, which can be modeled by stochastic algorithms. Hence these two examples are representative of two wide classes of materials, which differ for manufacturing processes and operating conditions. It is important to point out that the proposed micro-morphology techniques accurately recover the experimental values of permeability, without any special *ad-hoc* tuning. However, it must be recognized that the degree of clusterization in CL may depend on the assumptions made about the distribution of catalyst. For this reason, dif-

ferent catalytic distributions have been explored, in order to suggest that more realistic assumptions must be taken into account when dealing with CL, beyond standard approaches (simply based on Darcy's law).

Acknowledgements

Appendix A. Flow through array of body-centered cubic spheres (BCC)

In this Section, the hydraulic permeability associated with multiple ordered packs of identical spheres in a cubic domain was computed, by performing fluid flow simulations by LBM. In particular, body-centered cubic spheres (BCC) was considered [35] as shown in Fig. 8. A pressure gradient was applied along x-direction (see Fig. 8 for details) and the resulting steady-state averaged superficial velocity was used to calculate the permeability values, according to the Darcy's law.

Flow simulations with ordered packing of regular obstacles were performed to check the consistency of numerical predictions of permeability, obtained by different fluid dynamics softwares (PALABOS [58] and ANSYS Fluent® [59]) and analytic expressions from the literature. For validation purposes, the convenience of simulating ordered packs of spheres is twofold. First of all, exact analytic expressions are available. Secondly, adoption of periodic boundary conditions allows one to reduce the computational demand (in comparison with packs made of randomly placed spheres [14], where larger computational domains are typically required).

Permeability k is a constant factor appearing in the Darcy's law [55], which relates the pressure gradient ∇P across a porous medium to the volume averaged velocity u, i.e.,

$$u = -\frac{k\nabla P}{\mu},$$ (A.1)

where μ denotes viscosity. The volume averaged velocity, also called discharge per unit area, is not the velocity which fluid particles traveling through the pores is experiencing. In order to find out the latter quantity, the volume averaged velocity must be divided by the porosity to account for the fact that only a fraction of the total formation volume is available for flow.

Numerical results were compared to values as predicted by the analytic expressions (see [60, 61]). Prediction of permeability of porous media with periodic structures dates back to the theoretical works of Hasimoto [62], and later on, to the work of Sangani and Acrivos [60], which performed analytic and numerical studies of periodic arrays of spheres for different configurations. According to these models, the permeability can be computed as

$$k_S = \frac{R^2}{6\pi d_k}\left(\frac{L}{R}\right)^3,$$ (A.2)

where L is the edge of the periodic cell, R is the radius of the sphere and d_k is a dimensionless drag coefficient. The dimensionless drag coefficient d_k is determined by geometric parameters of the porous media, and can be represented by a power series of γ as follows

$$d_k = \sum_{n=0}^{30} q_n \gamma^n, \tag{A.3}$$

where the coefficients q_i are tabulated [60]. The dependence of the parameter γ on porosity ε takes into account the considered configuration, i.e. the spheres arrangement. For body-centered cubic (BCC) configuration, the dependence reads

$$\gamma = \left(\frac{8(1-\varepsilon)}{\sqrt{3}\pi}\right)^{1/3}. \tag{A.4}$$

It should be noted that this analytical model is accurate in the limits of low and high porosity. More specifically, analytic expression given by Hasimoto [62] is not valid for $\gamma \leq 0.2$, and in work by Sangani [60] authors improved this using the same method as Hasimoto, but adding extra terms in the velocity expression, with a wider validity range: $0 < \gamma < 0.85$. For high densities they obtained the lubrication type approximations for narrow gaps [63].

Another popular relation was proposed by Kozeny [64] and later modified by Carman [65]. The resulting equation is known as the Kozeny-Carman (KC) equation. Authors considered a porous material as an assembly of capillary tubes for which the equation of Navier-Stokes can be used. This yields the permeability k as a function of porosity ε, specific surface, and a factor accounting for the shape and tortuosity of channels. Since its first appearance in [65], this equation has taken several forms, including the following one

(Eq. A.5) that is commonly used for porous media with spherical particles
[61]:

$$k_{KC} = \frac{D^2}{150} \frac{\varepsilon^3}{(1 - \varepsilon)^2},$$ (A.5)

where D is the sphere diameter.

We notice that the estimates of permeability as predicted by Eq. (A.2) on (A.5) show a good agreement only for a small range of porosity, namely $\varepsilon \in [0.7; 0.82]$.

The convergence of permeability for ordered arrays of spheres has been analyzed as a function of mesh resolution. We have simulated a flow through idealized three-dimensional porous structures composed of ordered arrays of spheres with BCC packing configuration, by setting fixed pressure boundaries at inlet and outlet (along x-direction in Fig. 8). Sphere surfaces were treated as no-slip wall boundaries using the bounce-back boundary conditions (see previous Section). In this configuration, we considered a cubic unit cell with periodic boundary conditions along both y- and z-direction. Following [61], we adopted an edge of the periodic computational box with $L = 1.917\,cm = 1.917 \times 10^{-2}\,m$ and porosity $\varepsilon = 0.32$.

In order to validate the solver that is used in the rest of the paper, i.e. LBM solver with $D3Q19$ lattice implemented in PALABOS [58], different comparisons were carried out. In Table 7 the input parameters imposed in our simulations, as well as the obtained results, are presented. Values for permeability obtained by PALABOS were compared with (a) other LBM simulations [61], (b) results obtained by commercial software ANSYS Fluent[R] [59] and (c) analytic predictions by Kozeny-Carman equation (see Eq. (A.5)). In particular, the PALABOS results, as common in the LBM literature, are

expressed first in dimensionless units (so-called lattice units $l.u.$, see [23]) and then in physical units by means of proper scaling factors. For the sake of clarity, all these data are shown in Fig. 9 (inset), where good agreement is found. In LBM simulations by PALABOS, the relaxation parameter has been chosen as $\omega = 1.0$ $l.u.$ and the kinematic viscosity $\nu = 1/6$ $l.u.$ in order to minimize the effect of viscosity on permeability (see in particular Fig. 4 of Ref. [35]). This choice allows to obtain the maximum accuracy by means of the simplified BGK collisional model and to avoid the use of more complex collisional models, like the multiple-relaxation-time (MRT) model (see [46] and [14] for applications to PEM fuel cells).

In Table 8 the dependence of permeability on the numerical resolution, i.e. number of computational node for discretizing the box edge, is reported. Results clearly show a considerable dependency of permeability for coarser meshes, while a plateau is observed starting from a 256^3 resolution. Hence the 512^3 resolution can be considered accurate enough to get mesh-independent results.

Simulations were performed using a DELL Precision® T7500 Linux workstation with CPU Due Intel® Xeon® X5650 (six cores, clock rate 2.66 GHz, 12 MB cache) and 48 GB (6×8GB) of DDR3 memory (1333 MHz), with OS Red Hat Enterprise Linux version 6.3.

[1] J. Zhang, Z. Xie, J. Zhang, Y. Tang, C. Song, T. Navessin, Z. Shi, D. Song, H. Wang, D.P. Wilkinson, Z.-S. Liu, S. Holdcroft, High temperature PEM fuel cells, *Journal of Power Sources*, 2006, 160, 872-891

[2] T.J. Schmidt, J. Baurmeister, Properties of high-temperature PEFC

Celtec-P 1000 MEAs in start/stop operation mode, *Journal of Power Sources*, 2008, 176, 428-434

[3] C. Yang, S. Srinivasan, A.B. Bocarsly, S. Tulyani, J.B. Benziger, A comparison of physical properties and fuel cell performance of Nafion and zirconium phosphate/Nafion composite membranes, *J. Membr. Sci.*, 2004, 237, 145-161

[4] Y.S. Kim, F. Wang, M. Hickner, T.A. Zawodzinski, J.E. McGrath, Fabrication and characterization of heteropolyacid (H3PW12O40)/directly polymerized sulfonated poly(arylene ether sulfone) copolymer composite membranes for higher temperature fuel cell applications, *J. Membr. Sci.*, 2003, 212, 263-282

[5] F.N. Buchi, B. Gupta, O. Haas, G.G. Scherer, Study of radiation-grafted FEP-G-polystyrene membranes as polymer electrolytes in fuel cells, *Electrochim. Acta*, 1995, 40, 345-353

[6] H. Wang, G.A. Capuano, Behavior of Raipore Radiation-Grafted Polymer Membranes in H2/O2 Fuel Cells, *J. Electrochem. Soc.*, 1988, 145, 780-784

[7] D.A. Stevens, J.R. Dahn, Thermal degradation of the support in carbon-supported platinum electrocatalysts for PEM fuel cells, *Carbon*, 2005, 43, 179-188

[8] M.S. Wilson, F.H. Garzon, K.E. Sickafus, S. Gottesfeld, Surface Area Loss of Supported Platinum in Polymer Electrolyte Fuel Cells, *J. Electrochem. Soc.*, 1993, 140, 2872-2877

[9] T. Tada, High dispersion catalysts including novel carbon supports, in: Wolf Vielstich, Hubert, A. Gasteiger, Arnold Lamm (Eds.), Handbook of Fuel Cells - Fundamentals, Technology and Applications: Fuel Cell technology and Application, vol. 3, John Wiley and Sons, Ltd., 2003

[10] R.M. Darling, J.P. Meyers, Kinetic Model of Platinum Dissolution in PEMFCs, *J. Electrochem. Soc.*, 2003, 150, A1523-A1527

[11] H. Uchida, J.M. Song, S. Suzuki, E. Nakazawa, N. Baba, M. Watanabe, Electron Tomography of Nafion Ionomer Coated on Pt/Carbon Black in High Utilization Electrode for PEFCs, *Journal of Physical Chemistry B*, 2006, 110(27), 13319-13321.

[12] T. Ito, U. Matsuwaki, Y. Otsuka, G. Katagiri, M. Kato, K. Matsubara, Y. Aoyama, H. Jinnai, Direct Three-dimensional Visualization and Morphological Analysis of Pt Particles Supported on Carbon by Transmission Electron Micro-tomography, Wiley Online Library, 2010.

[13] Simon Thiele, Tobias Fürstenhaupt, Dustin Banham, Tobias Hutzenlaub, Viola Birss, Christoph Ziegler, Roland Zengerle. Multiscale tomography of nanoporous carbon-supported noble metal catalyst layers. *Journal of Power Sources*, 2013, 228, 185-192

[14] Y. Gao, X. X. Zhang, P. Rama, Y. Liu, R. Chen, H.Ostadi, K. Jiang, Modeling Fluid Flowin the Gas Diffusion Layers in PEMFC Using the Multiple Relaxation-time Lattice Boltzmann Method, *Fuel Cells*, 2012, 12:3, 365-381

[15] http://www.math2market.de

[16] S. Rief, E. Glatt and A. Wiegmann: Microstructure Simulation of Virtual Woven Filter Media, Filtech, Wiesbaden, Deutschland, Vol. 1, 2009, pp 231-238.

[17] E. Glatt, S. Rief, A. Wiegmann, M. Knefel and E. Wegenke. Structure and pressure drop of real and virtual metal wire meshes, Fraunhofer ITWM 157 (2009), ISSN: 1434-9973

[18] L. Cindrella, A.M. Kannan, J.F. Lin, K. Saminathan, Y. Ho, C.W. Lin, J. Wertz, Gas diffusion layer for proton exchange membrane fuel cells: A review, *Journal of Power Sources*, 2009, 194, 146-160

[19] F. J. Higuera, S. Succi, R. Benzi, Lattice Gas Dynamics with Enhanced Collisions, *EuroPhys. Lett.*, 1989, 9, 345-349

[20] F. J. Higuera, J. Jimenez, Boltzmann approach to lattice gas simulations, *EuroPhys. Lett.*, 1989, 9, 663-668

[21] H. Chen, S. Chen, H. W. Matthaeus, Recovery the Navier-Stokes equations using lattice gas Boltzmann method, *Phys. Rev. A*, 1992, 45, R5339-R5342

[22] Y. Qian, D. d'Humières, P. Lallemand, Lattice BGK models for Navier-Stokes equation, *Europhys.Lett.*, 1992, 17, 479-484

[23] S. Succi, The lattice Boltzmann equation for fluid dynamics and beyond, 2nd ed. Oxford University Press, New York, 2001

[24] X. He, L. S. Luo, Theory of lattice Boltzmann method: from the Boltz-

mann equation to the lattice Boltzmann equation, *Phys. Rev. E*, 1997, 56, 6811-6817

[25] M. Sbragaglia, S. Succi, A note on the lattice Boltzmann method beyond the Chapman-Enskog limits, *Europhys. Lett.*, 2006, 73:3, 370-376

[26] D. Raabe, Overview of the lattice Boltzmann method for nano- and microscale fluid dynamics in materials science and engineering, *Modelling Simul. Mater. Sci. Eng.*, 2004, 12, 77661-5

[27] T. Inamuro, T. Ogata, S. Tajima, S. Konishi, *J. Comput. Phys.*, 2004, 198, 628-644

[28] P. Asinari, M.R. von Spakovsky, M.Q. Calí, V.B. Kasula, Direct numerical calculation of the kinematic tortuosity of reactive mixture flow in the anode layer of solid oxide fuel cells by the Lattice Boltzmann Method, *Journal Of Power Sources*, 2007, 170, 359-375

[29] P.P. Mukherjee, Q. Kang and C.-Y. Wang, Pore-scale modeling of two-phase transport in polymer electrolyte fuel cells:progress and perspective, *Energy Environ. Sci.*, 2011, 4, 346-369

[30] D.F. Cheddie, N.D.H. Munroe, Three dimensional modeling of high temperature PEM fuel cells, *Journal of Power Sources*, 2006, 160, 215-223

[31] P. J. Dellar, An interpretation and derivation of the lattice Boltzmann method using Strang splitting, *Computers and Mathematics with Applications*, 2011,doi:10.1016/j.camwa.2011.08.047

[32] P. Bhatnagar, E. P. Gross, and M. K. Krook, A model for collision process in gases: i. small amplitude processes in charged and neutral one-component system, *Phys. Rev*, 1954, 94, 511

[33] S. Chapman and T. G. Cowling, The Mathematical Theory of Non-Uniform Gases, Cambridge University Press, 1970

[34] M. Junk, A. Klar, L.-S. Luo, Asymptotic analysis of the lattice Boltzmann equation, *J. Comput. Phys.*, 2005, 210:2, 676-704

[35] Ch. Pan, L. Lou, C.T. Miller, *Computers and Fluids*, 2006, 35, 898-909

[36] D. P. Ziegler, (1993). Boundary conditions for the lattice Boltzmann simulations. *J. Stat. Phys.*, 1993, 71:1171

[37] M. Bouzidi, M. Firdaouss and P. Lallemand, Momentum transfer of a Boltzmann-lattice fluid with boundaries, *Physics of fluids*, 2001, 13:11, 3452-3459

[38] J. Lobato, P. Canizares, M.A. Rodrigo, J.J. Linares, D. Ubeda, F.J. Pinar, Study of the catalytic layer in polybenzimidazole-based high temperature PEMFC: Effect of platinum content on the carbon support, *Fuel Cells*, 2010, 10:2, 312-319

[39] C. Siegel G. Bandlamudi, A. Heinzel, Systematic characterization of a PBI/H_3PO_4 sol-gel membrane: Modeling and simulation, *Journal of Power Sources*, 2011, 196, 2735-2749

[40] M. Kvesic, U. Reimer, D. Froning, L. L uke, W. Lehnert, D. Stolten, 3D

modeling of a 200 cm^2 HT-PEFC short stack, *International Journal of Hydrogen Energy*, 2012, 37, 2430-2439

[41] E. Antolini, Carbon supports for low-temperature fuel cell catalysts, *Applied Catalysis B: Environmental*, 2009, 88, 1-24

[42] A. Atkinson, S. Barnett, R.J. Gorte, J.T.S. Irvine, A.J. McEvoy, M. Mogensen, S.C. Singhal, J. Vohs, Advanced anodes for high-temperature fuel cells, Nature Materials, 2004, 3, 17-27

[43] A. Lanzini, P. Leone, P. Asinari, Microstructural characterization of solid oxide fuel cell electrodes by image analysis technique, *Journal of Power Sources*, 2009, 194, 408-422

[44] D.M. Gattia, M.V. Antisari, L. Giorgi, R. Marazzi, E. Piscopiello, A. Montone, S. Bellitto, S. Licoccia, E. Traversa, Study of different nanostructured carbon supports for fuel cell catalysts, *Journal of Power Sources*, 2009, 194, 243-251

[45] D. Stauffer, A. Aharony, Introduction to Percolation Theory, second ed., Taylor and Francis, London, 1994, 89-103

[46] D. d'Humières. Generalized lattice Boltzmann equations, in: B.D. Shizgal, D.P. Weaver (Eds.), *Rarefied Gas Dynamics: Theory and Simulations, in: Prog. Astronaut. Aeronaut.*, 1992, 159:450

[47] G. Wellein, T. Zeiser, G. Hager, S. Donath, On the single processor performance of simple lattice Boltzmann kernels, *Computers & Fluids*, 2006, 35, 910919

[48] D. Groen, *et al.*, Analysing and modelling the performance of the HemeLB lattice-Boltzmann simulation environment, *J. Comput. Sci.*, 2013, http://dx.doi.org/10.1016/j.jocs.2013.03.002

[49] Y. Sone, Kinetic Theory and Fluid Dynamics, second ed., Birkhäuser, Boston, 2002

[50] H. Struchtrup, Macroscopic Transport Equations for Rarefied Gas Flows: Approximation Methods in Kinetic Theory, Interaction of Mechanics and Mathematics Series, Springer, Heidelberg, 2005.

[51] C. Cercignani, The Boltzmann Equation and Its Applications, New York, Springer- Verlag, 1988.

[52] G. Karniadakis, A. Beskok, N. Aluru, Microflows and Nanoflows: Fundamentals and Simulation, Springer, 2005.

[53] R.B. Bird, E. Lightfoot, Transport Phenomena, John Wiley & Sons, New York, 1960.

[54] E.W. Lemmon, M.O. McLinden, D.G. Friend, Thermophysical properties of fluid systems, in: P.J. Linstrom, W.G. Mallard (Eds.), NIST Chemistry WebBook, National Institute of Standards and Technology, 2003.

[55] G.K. Batchelor, An Introduction to Fluid Dynamics, Cambridge University press, Cambridge, 1967

[56] R.J.M. De Wiest, Flow through porous media, Academic Press, New York and London, 1969.

[57] E.B. Arkilic, M.A. Schmidt, and K.S. Breuer, Gaseous slip flow in long microchannels,*Journal of Micromechanical Systems*, 1997, 6, 167-178

[58] http://www.palabos.org

[59] http://www.ansys.com

[60] A.S. Sangani, A. Acrivos, Slow flow through a periodic array of spheres, *Int. J. Multiph. Flow*, 1982, 8, 343-360

[61] M.L.Stewart, A.L.Ward, D.R.Rector, A study of pore geometry effects on anisotropy in hidraulic permeability using lattice-Boltzmann method, *Advances in Water Resources*, 2006, 29, 1328-1340

[62] H. Hasimoto, On the periodic fundamental solutions of the Stokes equations and their application to viscous flow past a cubic array of spheres, *J. Fluid Mech.*, 1959, 5, 317-328

[63] K. Yazdchi, S. Srivastava, S. Luding, Microstructural effects on the permeability of periodic fibrous porous media, *Int. J. of Multiphase Flow*, 2011, 37, 956-966

[64] J. Kozeny, Ueber kapillare Leitung des Wassers im Boden, Sitzungsber Akad. Wiss., Wien, 1927, 136:2a, 271-306

[65] P.C. Carman, Fluid flow through granular beds, Transactions, Institution of Chemical Engineers, London, 1937, 15, 150-166

List of Tables

Table 1: Typical transport parameters of the GDL and CL of a HT-PEM fuel cell from literature.

Parameter	Value	Reference
l_{GDL}	$400\,\mu m$	Siegel [39]
ε_{GDL} (BASF Celtec-P 1000)	0.7	Kvesic [40]
k_{GDL} (BASF Celtec-P 1000)	$10^{-12}\,m^2$	Kvesic [40]
ε_{GDL} (BASF Celtec-P 2000)	0.78	Siegel [39]
k_{GDL} (BASF Celtec-P 2000)	$5 \times 10^{-13}\,m^2$	Siegel [39]
$l_{CL,a}$	$30\,\mu m$	Siegel [39]
$l_{CL,c}$	$40\,\mu m$	Siegel [39]
Carbon support particle size	$30 - 40\,nm$	Antolini [41]
ε_{CL}	$0.5 - 0.6$	Lobato [38]
k_{CL} (BASF Celtec-P 2000)	$1 \times 10^{-13}\,m^2$	Siegel [39]

Table 2: Numerical results of permeability of GDL (*l.u.* stands for lattice units, see [23]).

Resolution	$432 \times 1112 \times 1112$
Lattice average velocity	$3.60172 \times 10^{-07} \, l.u.$
Lattice pressure gradient	$1.16009 \times 10^{-07} \, l.u.$
Lattice length	$9.259 \times 10^{-07} \, m$
Actual permeability	$0.443638 \times 10^{-12} \, m^2$

Table 3: Sensitivity of permeability on the cluster size of carbon particles in CL ($l.u.$ stands for lattice units, see [23]).

Resolution	$200 \times 200 \times 200$
Average size of cluster	$40\,nm$
Lattice average velocity	$1.60371 \times 10^{-05}\,l.u.$
Lattice pressure gradient	$2.51256 \times 10^{-06}\,l.u.$
Lattice length	$1.0 \times 10^{-08}\,m$
Actual permeability	$1.07451 \times 10^{-16}\,m^2$
Resolution	$200 \times 200 \times 200$
Average size of cluster	$400\,nm$
Lattice average velocity	$7.16111 \times 10^{-04}\,l.u.$
Lattice pressure gradient	$2.51256 \times 10^{-06}\,l.u.$
Lattice length	$1.0 \times 10^{-08}\,m$
Actual permeability	$0.47502 \times 10^{-14}\,m^2$
Resolution	$400 \times 400 \times 400$
Average size of cluster	$1500\,nm$
Lattice average velocity	$1.26456 \times 10^{-04}\,l.u.$
Lattice pressure gradient	$1.25313 \times 10^{-06}\,l.u.$
Lattice length	$5.0 \times 10^{-08}\,m$
Actual permeability	$0.420467 \times 10^{-13}\,m^2$

Table 4: Estimation of mean free paths for the gases involved in electrochemical reactions of the HT-PEM. Operating temperature $T = 423\,K$ and pressure $P = 101325\,Pa$. Data taken from Ref. [54].

	Oxygen	Hydrogen	Water (vapor)
Molecular weight	$0.032\,kg/mol$	$0.002\,kg/mol$	$0.018\,kg/mol$
Molecular mass	$5.314 \times 10^{-26}\,kg$	$3.321 \times 10^{-27}\,kg$	$2.989 \times 10^{-26}\,kg$
Dynamic viscosity	$2.67 \times 10^{-05}\,Pa\,s$	$1.13 \times 10^{-05}\,Pa\,s$	$1.42 \times 10^{-05}\,Pa\,s$
Density	$0.973\,kg/m^3$	$0.061\,kg/m^3$	$0.547\,kg/m^3$
Kinematic viscosity	$2.75 \times 10^{-05}\,m^2/s$	$1.86 \times 10^{-04}\,m^2/s$	$2.60 \times 10^{-05}\,m^2/s$
Mean free path λ	$159\,nm$	$270\,nm$	$113\,nm$

Table 5: Estimate of rarefaction effects for hydrogen gas flow, with mean free path $\lambda = 270\,nm$ (see Table 4), through GDL and CL.

Layer	ε	$k_{no-slip}$	L_{char}	Kn	$k_{slip}/k_{no-slip}$
GDL	0.7	$0.443638 \times 10^{-12}\,m^2$	$7.12 \times 10^{-6}\,m$	0.038	1.455
CL	0.5	$0.420467 \times 10^{-13}\,m^2$	$2.59 \times 10^{-6}\,m$	0.104	2.249

Table 6: Simulation results and comparison.

Name	Non-distributed	Distributed
Average size of clusters	1500 nm	1500 nm
Relaxation frequency	1.1 $l.u.$	1.1 $l.u.$
Lattice viscosity	0.136364 $l.u.$	0.136364 $l.u.$
Δ P	1.0×10^{-5} $l.u.$	1.0×10^{-5} $l.u.$
Domain size	$128 \times 128 \times 128$	$128 \times 128 \times 128$
Flow rate	3.06678×10^{-7} $l.u.$	2.22284×10^{-6} $l.u.$

Table 7: Input parameters and obtained numerical results by ANSYS Fluent$^{\circledR}$, PALA-BOS, literature [61] and Kozeny-Carman model. The PALABOS results are reported first in dimensionless units (the so-called lattice units $l.u.$, see [23]) and then in physical units.

Parameters	
Porosity	0.32
R/L ratio	0.433
Sphere diameter D	0.0166 m
Edge of computational box L	0.01917 m
ANSYS Fluent$^{\circledR}$	
Dynamic viscosity	0.001 $kg/(m \times s)$
Pressure gradient ∇P	0.245 Pa/m
Average pore velocity	0.7970 $\times 10^{-04}\, m/s$
Surface velocity	0.3276 $\times 10^{-04}\, m/s$
Mass flow rate	0.1192 $\times 10^{-04}\, kg/s$
Permeability-FLUENT	$\boxed{1.337 \times 10^{-07}\, m^2}$
PALABOS	
Resolution	$512 \times 512 \times 512$
Lattice viscosity ν	$1/6\, l.u.$
Lattice pressure gradient	$9.78474 \times 10^{-08}\, l.u.$
Lattice average velocity	$5.32578 \times 10^{-05}\, l.u.$
Lattice permeability	$90.7158\, l.u.$
Permeability-PALABOS	$\boxed{1.2757 \times 10^{-07}\, m^2}$
OTHERS	
Permeability [61]	$\boxed{1.240 \times 10^{-07}\, m^2}$
Permeability Eq. (A.5)	$\boxed{1.302 \times 10^{-07}\, m^2}$

Table 8: Dependence of permeability on resolution. The results are reported first in dimensionless units (the so-called lattice units $l.u.$, see [23]) and then in physical units.

Resolution	$64 \times 64 \times 64$
Lattice average velocity	$3.68895 \times 10^{-05}\, l.u.$
Lattice pressure gradient	$7.93651 \times 10^{-06}\, l.u.$
Lattice permeability	$0.77468\, l.u.$
Actual permeability	$0.697212 \times 10^{-07}\, m^2$
Resolution	$128 \times 128 \times 128$
Lattice average velocity	$1.04201 \times 10^{-5}\, l.u.$
Lattice pressure gradient	$3.93701 \times 10^{-06}\, l.u.$
Lattice permeability	$4.41116\, l.u.$
Actual permeability	$0.992511 \times 10^{-07}\, m^2$
Resolution	$256 \times 256 \times 256$
Lattice average velocity	$4.91507 \times 10^{-06}\, l.u.$
Lattice pressure gradient	$3.92157 \times 10^{-08}\, l.u.$
Lattice permeability	$20.889\, l.u.$
Actual permeability	$1.175006 \times 10^{-07}\, m^2$
Resolution	$512 \times 512 \times 512$
Lattice average velocity	$5.32578 \times 10^{-05}\, l.u.$
Lattice pressure gradient	$9.78474 \times 10^{-08}\, l.u.$
Lattice permeability	$90.7158\, l.u.$
Actual permeability	$1.275691 \times 10^{-07}\, m^2$

List of Figures

(a) HT-PEM Fuel Cell

(b) Gas diffusion layer (GDL)

(c) Catalyst layers (CL) + Membrane
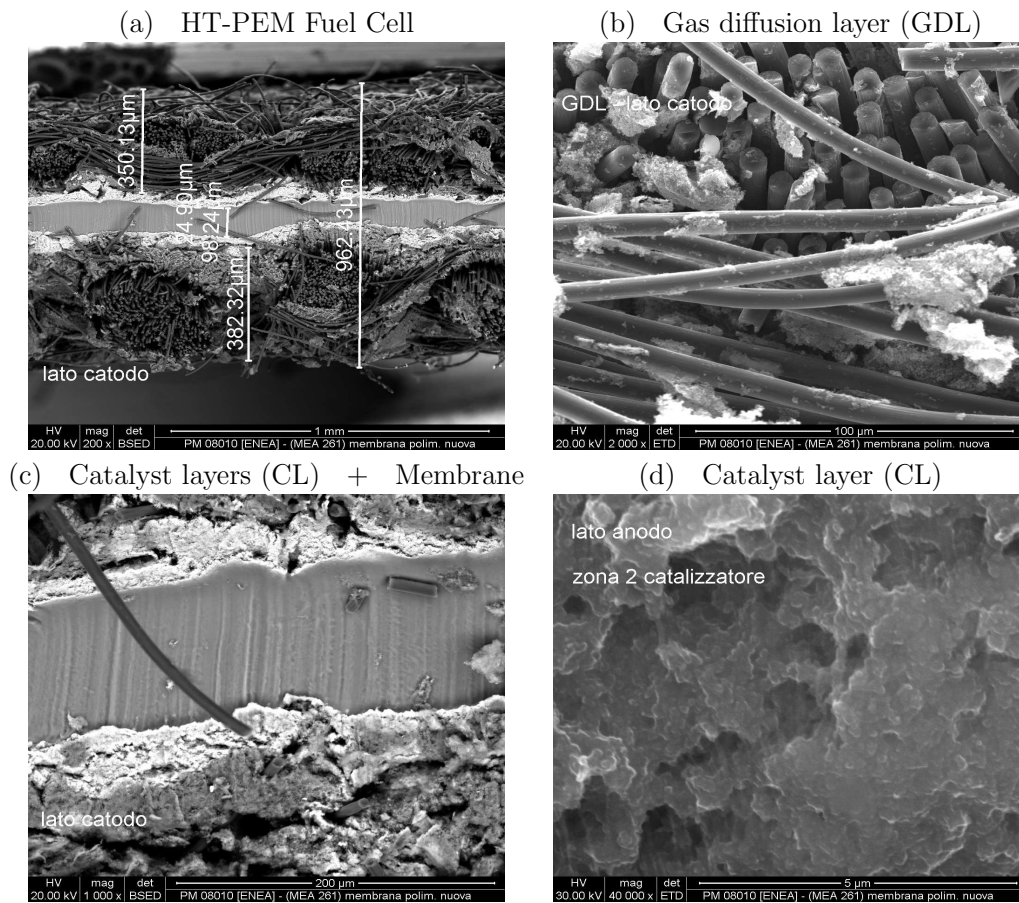
(d) Catalyst layer (CL)

Figure 1: Micro-morphology of a HT-PEM fuel cell by Scanning Electron Microscope (SEM) imaging (purposely obtained for the present work).
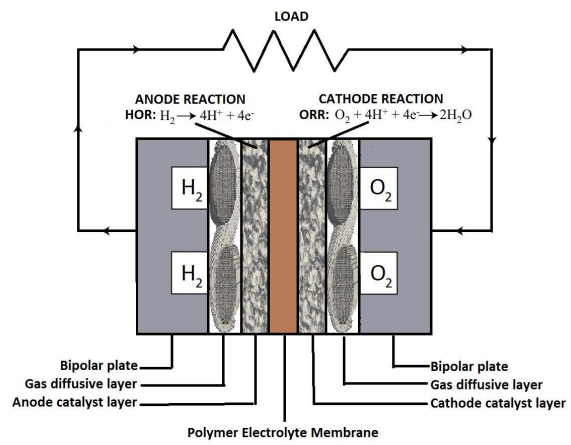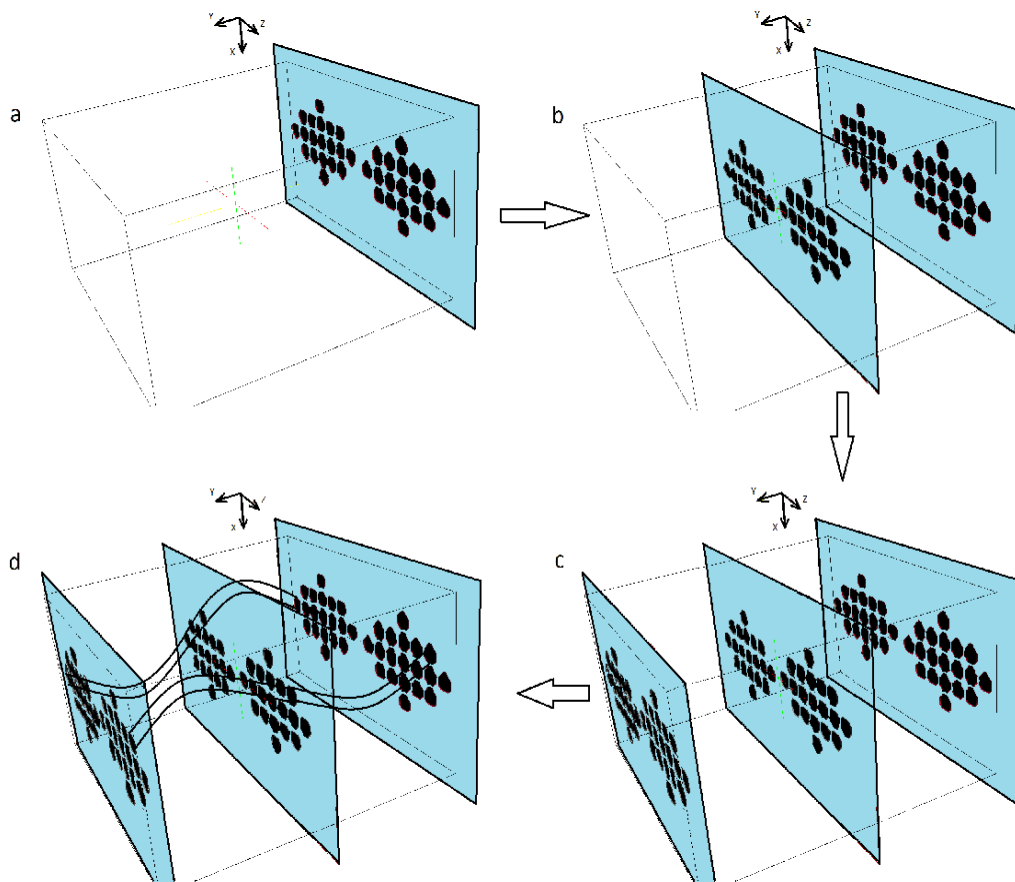
Figure 2: Schematic diagram of PEMFC.
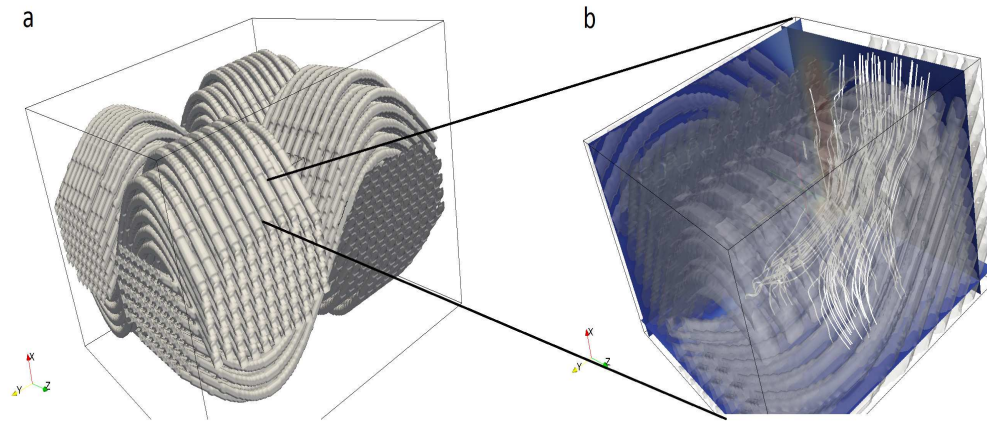
Figure 3: Reconstruction steps of a woven GDL.

Figure 4: Geometry of the reconstruction and streamlines of fluid flow through a woven GDL. In order to simplify the visualization, the used parameters, namely $N_A = 6$, $N_B = 4$, $N_x = 180$ and $N_y = N_z = 240$, are coarser than those required by computing permeability.
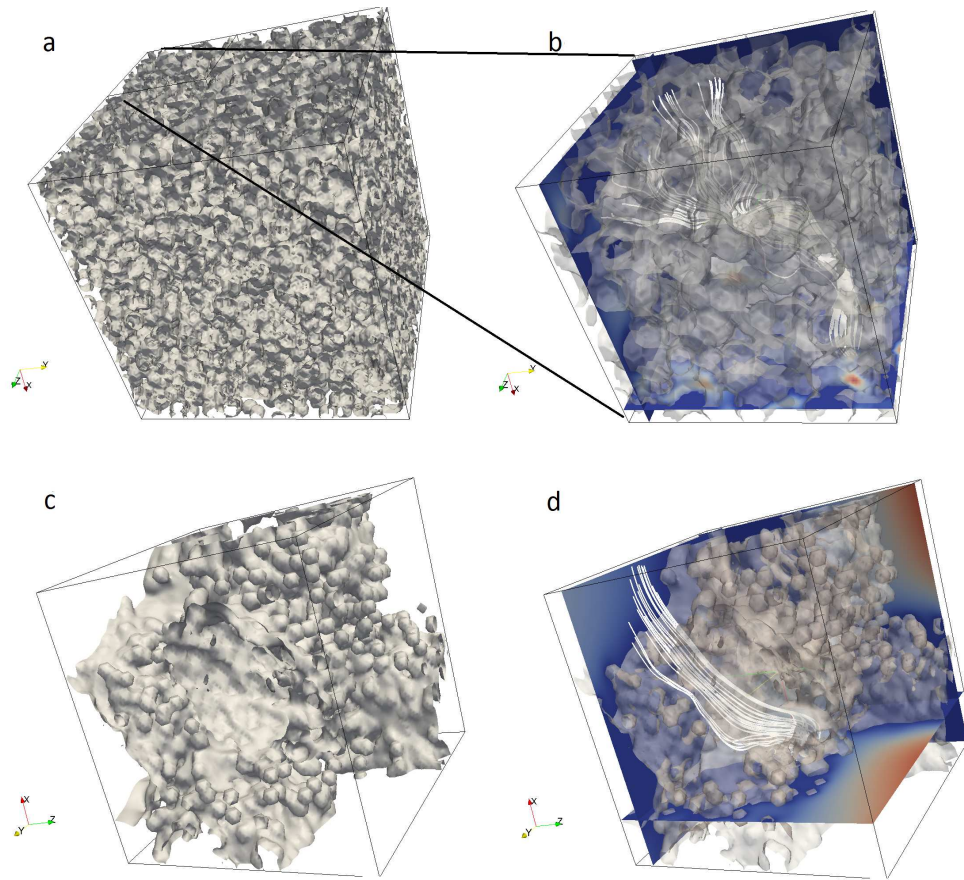
Figure 5: The geometry and flow streamlines through reconstructed CL porous medium: (a)-(b) the results of the straightforward algorithm; (c)-(d) the results of clusterization one for $L_{cluster}^{av} = 350\,nm$.

60
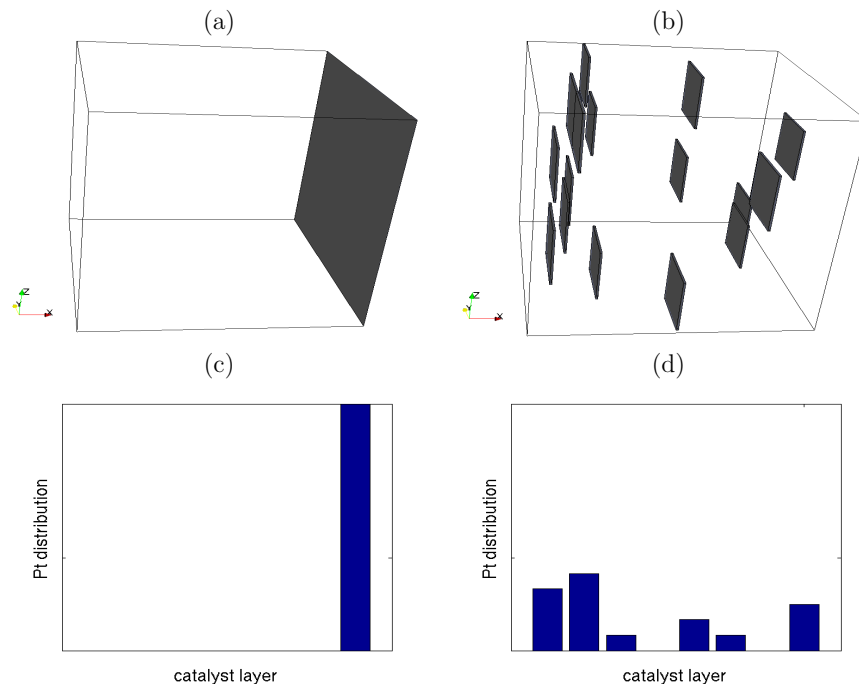
Figure 6: Two considered (a-b) locations and (c-d) corresponding deposition distribution of Pt particles inside the catalyst layer.
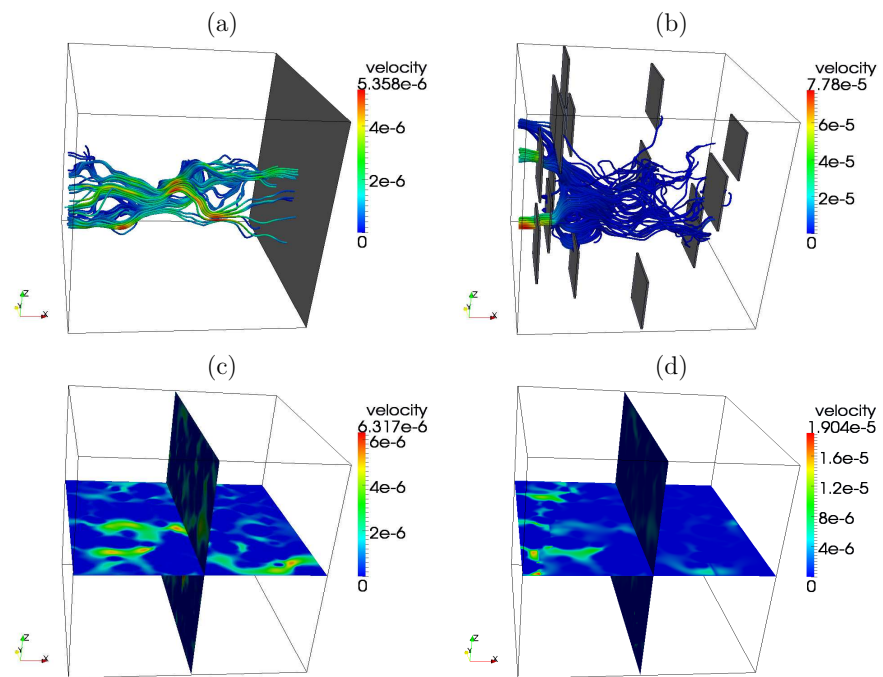
Figure 7: (a-b) Pt deposition and flow streamlines (c-d) slices of corresponding flow velocity
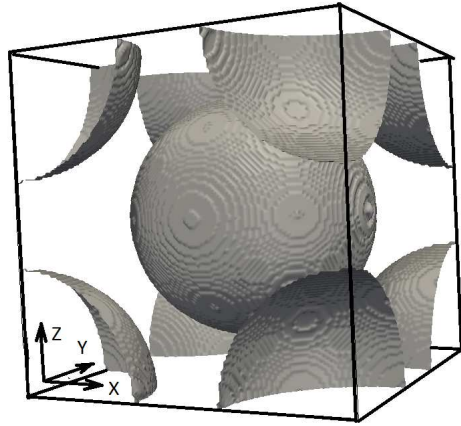
Figure 8: Periodic unit cell of an infinite array of body-centered cubic spheres.
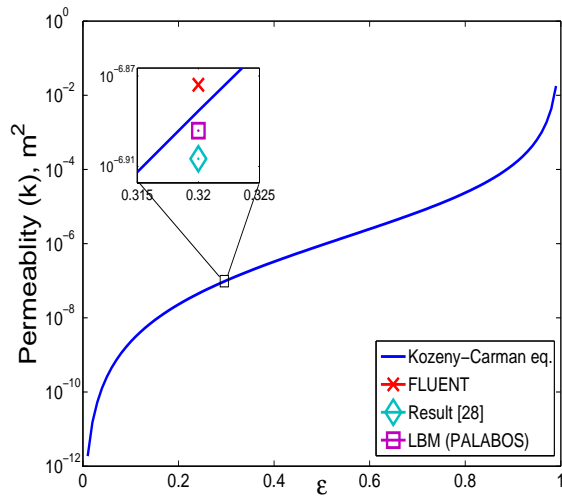
Figure 9: Permeability as a function of porosity given by Eq. (A.5). Inset: The results of different numerical methods for porosity $\varepsilon = 0.32$.